IOPscience iopscience.iop.org

Home Search Collections Journals About Contact us My IOPscience

An optical study of the lateral motion of two-dimensional electron-hole pairs in GaAs/AlGaAs quantum wells

This article has been downloaded from IOPscience. Please scroll down to see the full text article.

1993 J. Phys.: Condens. Matter 5 5563

(http://iopscience.iop.org/0953-8984/5/31/019)

View the table of contents for this issue, or go to the journal homepage for more

Download details:
IP Address: 171.66.16.96
The article was downloaded on 11/05/2010 at 01:35

Please note that terms and conditions apply.

J. Phys.: Condens. Matter 5 (1993) 5563–5580. Printed in the UK

An optical study of the lateral motion of two-dimensional electron–hole pairs in GaAs/AlGaAs quantum wells*

H Hillmer†, A Forchel‡ and C W Tu§||

† DBP Telekom, Forschungs- und Technologiezentrum, Postfach 10 00 03, D-6100 Darmstadt, Federal Republic of Germany

‡ Technische Physik, Universität Würzburg, Am Hubland, D-8700 Würzburg, Federal Republic of Germany

§ AT&T Bell Laboratories, Murray Hill, NJ 07974-2070, USA

Received 22 March 1993, in final form 13 May 1993

Abstract. We have studied the lateral transport of electron–hole (e–h) pairs in $GaAs/Al_xGa_{1-x}As$ quantum wells (QWs) ($0.3 \leqslant x \leqslant 1.0$) as a function of well width, temperature and Al content in the barriers by a method based on transparent circular microstructured areas in otherwise opaque masks. In the experiment we observe an increase of the e–h-pair mobilities with both growing Al content and increasing well width. The experimental results are compared with theoretical model calculations for different scattering mechanisms such as acoustic-deformation-potential (AC), polar-optical (PO), barrier-alloy-disorder (BAL), impurity and interface-roughness (IR) scattering. For low temperatures (about 40 K $< T <$ 90 K) the increase observed in the experiment can most probably be related to efficient IR scattering. Model calculations of IR scattering were used to determine approximately the geometrical roughness parameters of the interfaces. Based on this analysis, our samples investigated in this paper show average terrace heights of one monolayer, independent of well width. BAL scattering is found to affect the mobility of e–h pairs only for very narrow QWs at temperatures close to 100 K. At higher temperatures $T >$ 100 K AC scattering and PO scattering are found to dominate the scattering processes. In addition, a crossing of the theoretical electron and hole mobilities is observed for isolated BAL scattering for very narrow well widths or very low Al contents.

1. Introduction

The lateral motion of two-dimensional (2D) carriers confined in semiconductor heterostructures has been studied in detail experimentally and theoretically in recent years. Unipolar mobilities have been extensively studied in several material systems and for various geometrical configurations (see, e.g., [1–5]) using different experimental methods. The results have been compared to theoretical mobilities for electrons or holes which were calculated including different scattering mechanisms. The variations of the experimental mobilities with temperature were often used to identify the contributions of the different scattering mechanisms. In contrast, investigations of the lateral motion of ambipolar carriers were rather rare [6–11].

This paper reports experimental mobility data for the lateral motion of electron–hole (e–h) pairs in $GaAs/Al_xGa_{1-x}As$ quantum well (QW) structures. These data are compared

* The experimental work was performed at 4. Physikalisches Instutit, Universität Stuttgart, D-7000 Stuttgart-80, Pfaffenwaldring 57, Federal Republic of Germany.

|| Present address: Department of Electrical and Computer Engineering, University of California, San Diego, La Jolla, CA 92093-0407, USA.

0953-8984/93/315563+18$07.50 © 1993 IOP Publishing Ltd

with theoretical mobilities calculated for different scattering mechanisms such as acoustic-deformation-potential (AC), polar-optical (PO), barrier-alloy-disorder (BAL), impurity and interface-roughness (IR) scattering. A wide range of alloy compositions (Al content, $0.3 \leqslant x \leqslant 1.0$), well widths ($1 \text{ nm} \leqslant L_z \leqslant 20 \text{ nm}$) and temperatures ($40 \text{ K} \leqslant T \leqslant 200 \text{ K}$) are covered in this paper.

In section 2 the experimental method and the evaluation of the experimental data are briefly described and some results are displayed. Experimental e–h-pair mobilities as a function of well width, composition and temperature are discussed in section 3 in terms of different scattering mechanisms such as AC, PO and BAL scattering. At low temperatures the well width dependence of IR scattering is studied. Geometrical IR parameters are determined by fitting the results of IR model calculations to our experimental data.

2. Experimental method and evaluation of the experimental data

The samples have been grown by molecular beam epitaxy (MBE) on (100) oriented semi-insulating GaAs substrates and contain single QWs of different well widths. The first sample reveals an Al content of 0.37. The following layers have been grown in sequence on the substrate: a 500 nm thick GaAs buffer layer, a 100 nm thick $Al_{0.37}Ga_{0.63}As$ barrier layer, a GaAs QW of 10 nm width, a 30 nm thick $Al_{0.37}Ga_{0.63}As$ barrier, a 5 nm GaAs QW, 30 nm $Al_{0.37}Ga_{0.63}As$, a 2.5 nm GaAs QW, 30 nm $Al_{0.37}Ga_{0.63}As$, a 1.5 nm GaAs QW, and finally a 100 nm thick $Al_{0.37}Ga_{0.63}As$ cap layer. The second sample reveals an Al content of 0.3 and includes the following layers, in sequence: the substrate, a 245 nm thick $Al_{0.3}Ga_{0.7}As$/GaAs superlattice buffer layer, a 100 nm thick $Al_{0.3}Ga_{0.7}As$ barrier layer, a 20 nm GaAs QW, a 30 nm $Al_{0.3}Ga_{0.7}As$ barrier, a 10 nm GaAs QW, a 30 nm $Al_{0.3}Ga_{0.7}As$ barrier and finally a 5 nm GaAs cap layer. The samples include different well widths which guarantee identical growth conditions for these QWs having the same barrier Al content. Since the single QWs are embedded between relatively thick barrier layers, tunnelling of electrons and holes into neighbouring wells can be neglected.

We use a transport method capable of achieving an ultra-high resolution ($\simeq 0.1\ \mu$m) in space and a high resolution in time. Circular areas (holes) inside an opaque NiCr mask were applied, which are transparent for both the laser excitation light and the photoluminescence of e–h pairs confined in single QW structures. The optical excitation energy and density by short dye laser pulses (≈ 8 ps) is sufficiently low so that only e–h pairs are generated in the QWs inside the circular area. We verified that the QW emission intensity is proportional to the optical excitation intensity and to the carrier concentration. Thus, the QW emission can be used for the spatial and temporal probing of the lateral e–h pair diffusion in the QWs. Recording the QW emission from the circular area as a function of time, the evolution of the carrier concentration inside the hole area can be measured. Those e–h pairs which move under opaque parts of the mask during their lifetime do not contribute to the detectable emission. We have chosen hole radii of 2 μm which are comparable to the carrier diffusion lengths, to obtain a high sensitivity of our method for lateral carrier motion. Therefore, the time-resolved emission from the circular area includes information about important transport properties such as the diffusivity and the mobility. These properties can be extracted by the evaluation of measured temporal intensity profiles as a function of both temperature and well width. A detailed description of our method and the experimental set-up is included in [7].

In a first step, the time-resolved intensity variations are recorded without a mask coverage to determine the experimental carrier lifetime as a function of QW width and

temperature. Since the carrier density will decrease after the pulsed optical excitation it is important for our method that the carrier lifetime is independent of the excitation intensity (e–h pair density). We have checked that the decay of the radiative emission is monoexponential and independent of the e–h pair density at low densities ($\lesssim 10^{16}$ cm^{-3}). We chose very weak optical excitation corresponding to about 5×10^{15} cm^{-3} for the initial carrier concentration. This allows us to use in our evaluation a linear recombination term which includes an effective experimental lifetime†. The experimental e–h pair lifetime includes radiative and possible non-radiative recombination channels.

In a second step, masks of 2 μm hole radius are used for the experiments. Under these conditions the decay of the recorded emission, in addition, is strongly influenced by carrier transport under masked sample parts. The experiments on the masked samples were carried out under the same experimental conditions (e.g. excess excitation energy, excitation density, and laser focus) to control carefully the initial carrier concentration. The 2D diffusion equation including a diffusion and a linear recombination term with the experimental lifetime τ is used to describe the e–h-pair concentration $c(x, y, t)$ as a function of space and time:

$$\partial c/\partial t = D(\partial^2 c/\partial x^2 + \partial^2 c/\partial y^2) - c/\tau. \tag{1}$$

We consider isothermal diffusion neglecting temperature gradients which would lead to thermodiffusion contributions. Due to the ns timescale relevant for the diffusion, the photoexcited carriers can be assumed to be thermalized since the thermalization involves a timescale of a few ps or less. Thus, we approximate the carrier temperature by the lattice temperature.

Since the samples are nominally undoped and the NiCr masks are not directly evaporated on the sample surfaces [7] we believe that the residual electric fields are very weak and may only cause weak band bendings. Therefore thermal emission [12] of carriers into the barriers may be rather weak for the temperature range considered in this paper‡. Therefore, vertical carrier motion is neglected in (1).

The solution of (1) is obtained numerically, taking into account the initial conditions. The diffusivity is the only free parameter in this equation since the measured carrier lifetimes are used for τ. The curve fitting of the theoretical profiles to the experimental curves provides the diffusivity as a function of temperature and well width. For the low carrier densities considered here, the diffusivities $D(L_z, T)$ can be converted into mobilities $\mu(L_z, T)$ using the Einstein relation $\mu(L_z, T) = D(L_z, T)e/kT$. The elementary charge is given by e.

An example of experimental mobilities obtained for two GaAs QWs of $L_z = 10$ nm well widths confined by $Al_{0.3}Ga_{0.7}As$ or $Al_{0.3}Ga_{0.63}As$ barriers is depicted in figure 1 as a function of temperature. We observe a strong dependence of the diffusivities on temperature and

† Note that for high carrier concentrations a linear recombination term would not be valid due to, e.g., hyperbolic decay of the emission, many-body effects and Auger recombination.

‡ We believe that at higher temperatures the thermal emission of carriers into the barrier is very important. The experimental data in [12] have been acquired for, e.g., 200 K, which just corresponds to the upper border of the temperature range we consider in our paper. However, external electric fields have been applied in [12] that considerably modify the band structure and facilitate emission of carriers into the barriers. If thermal emission were strongly noticeable in our experiment we should observed decreasing diffusivities with increasing high temperatures, due to both smaller diffusivities in the barriers and the time required for the emission and recapture. However, the opposite behaviour is observed in our experiments: we found increasing diffusivities for temperatures increasing above 180 K [13, 14]. Thus, we think that our experimental data are not noticeably influenced by thermal emission of carrier pairs into the barriers. Therefore, vertical transport as well as tunnelling (due to the relatively thick AlGaAs barrier layers) is not considered in (1).

increased diffusivities for the higher Al content ($x = 0.37$). In addition, the dependence of the experimental mobility on well width and temperature is shown in figure 2 by the points. The Al content in the barriers is 0.37. With rising temperature we observed increasing mobilities in the low-temperature range. After passing a maximum the mobilities decrease again at higher temperatures. In addition, a strong increase of the mobilities is observed with growing well width.

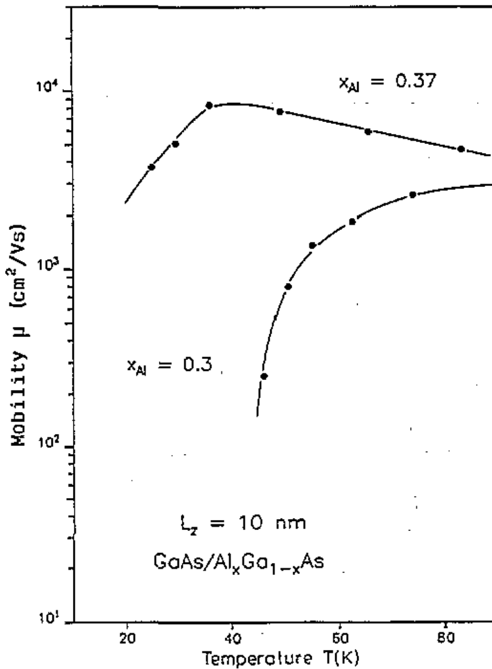

Figure 1. Mobilities of e–h pairs in GaAs/AlGaAs as a function of temperature for two different barrier compositions (Al content $x = 0.3$ and 0.37). The full curves are drawn to guide the eye.

3. Scattering mechanisms

This section deals with different scattering mechanisms which are discussed in order to provide a possible explanation for the variation of the experimental mobility of e–h pairs in GaAs/AlGaAs QWs with well width, Al content and temperature. In the following the influence of AC, PO, BAL, impurity and IR scattering will be studied.

Figure 2 depicts for each QW width (L_z = 1.5, 2.5, 5 and 10 nm) as a function of temperature a quantitative comparison between the experimental mobility and different calculated mobility limits (as explained below). Note that the plotted mobility range (vertical axis) is identical for the four parts of the figure. In the following we will discuss the contribution of several scattering mechanisms in order to provide a possible explanation for the variation of the experimental mobility data with temperature, well width and Al content.

Our simple model calculations [7] indicate that AC scattering reveals much higher mobilities in the single-particle condition (ambipolar limit) compared to the excitonic scattering condition. That means that excitons are less mobile than e–h pairs if only AC scattering is considered. Comparing the absolute values of these mobility calculations with experimental data (e.g. in figure 2) we found that the experiment can be much better described by the excitonic scattering condition. This was observed for all our studied

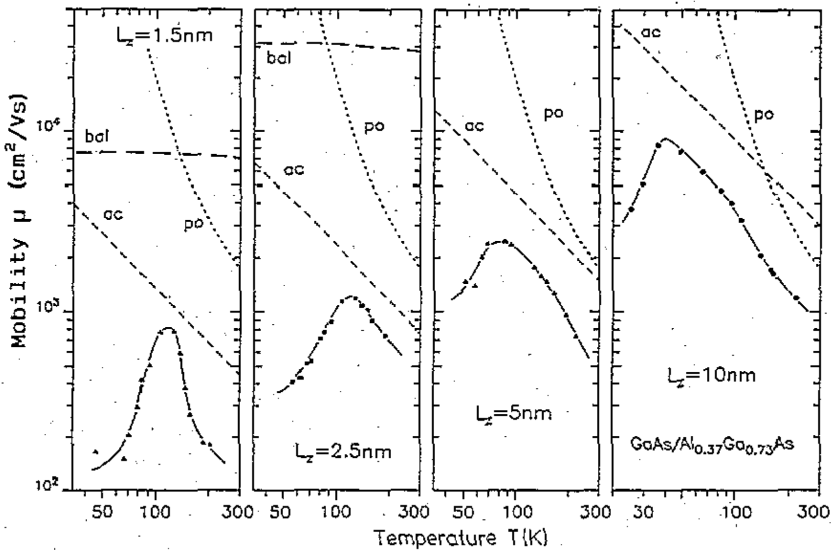

Figure 2. Temperature dependence of experimental and theoretical exciton mobilities for four different QW widths. The results for each well are displayed in a separate diagram. The experimental data given by symbols are connected by a full curve which is drawn to guide the eye. Calculated mobility variations are shown for AC scattering (short-dashed line), BAL scattering (long-dashed curve) and PO scattering (dotted curve). The strong well width dependence of the mobilities for low temperatures can be attributed to IR scattering.

samples having Al contents of 0.3, 0.37, 0.5 and 1.0. The excitonic scattering limit for AC scattering is displayed in figure 2 by the short-dashed line and is indicated by 'ac'. AC scattering shows a strong dependence on well width and temperature: $\mu_{ac} \propto L_z/T$ [7]. The better agreement between the excitonic limit and the experimental data indicates that for our experimental conditions the e–h pairs may be predominantly in the phase of excitons in the temperature range where AC scattering dominates.

For increasing temperatures the experimental mobilities decrease more strongly than the calculated limits of μ_{ac} predict. This deviation is most probably due to PO scattering which becomes dominant in that temperature range. We have calculated [7] PO scattering mobilities for 3D e–h pairs and 3D optical phonons according to [15]. Also in this case the excitonic limit describes the experimental data much better than the single-particle condition, which also indicates that excitons dominate for this temperature range. This was also found for PO scattering in $GaAs/Al_{0.5}Ga_{0.5}As$ QW structures, which have been studied in [7]. The excitonic mobility limits for the PO scattering are given by the dotted curve and are denoted by 'po'. However, according to figure 2, a small reduction of the PO scattering limited mobility with decreasing well width would be consistent with the experimental data. This indicates a possible well width dependence of PO scattering which, however, would be in contradiction to the reverse but weak dependence calculated in [9].

In the following the influence of BAL scattering on the lateral motion of e–h pairs in $GaAs/Al_xGa_{1-x}As$ QWs will be studied. From a microscopic point of view the random distribution of the group III elements Al and Ga in the barrier material $Al_xGa_{1-x}As$ causes a fluctuating potential. In this geometrical situation the efficiency of alloy-disorder scattering is determined among other points by the amount of the penetration of the electron and hole

wavefunctions into the barriers. In the following we show the results of a BAL scattering model calculation for the electron, hole and ambipolar mobility. Our QWs are modelled by rectangular finite symmetric electron and hole potential wells. The energy eigenvalues and respective wavefunctions $\Psi_i(z)$ are obtained by solving the Schrödinger equation for this problem (details are shown in appendix A). The BAL scattering rates and mobilities are calculated according to appendix B and appendix A. For the mobility of electrons ($i = \mathrm{e}$) and hole ($i = \mathrm{h}$) we find finally

$$\mu_i^{-1} = \frac{\pi^2}{e\hbar^3} n_0 m_{i,\mathrm{q},\|} m_{i,\mathrm{b},\|} V_{0,i}^2 x(1-x) 2 \int_{L_z/2}^{\infty} \left(\int_{-r_0}^{r_0} |\Psi_i(z+z_k)|^2 (r_0^2 - z^2)\, \mathrm{d}z \right)^2 F(T)\, \mathrm{d}z_k. \tag{2}$$

The factor $n_0 = 4/a^3$ gives the number of As atoms per unit volume a^3 and includes the lattice constant a; $m_{i,\mathrm{q},\|}$ ($m_{i,\mathrm{b},\|}$) denotes the GaAs QW ($Al_xGa_{1-x}As$ barrier) mass parallel to the interfaces, $V_{0,i}$ is the BAL scattering potential, and r_0 the radius of the Wigner–Seitz cell. The factor $F(T)$ contains the temperature dependence which originates from the energy averaging of the product of scattering rate and the occupation probability of the final scattering state. Scattering of electrons and holes will be mainly treated in the following and the ambipolar approximation will be applied first. Possible modifications for excitons will be discussed second. Details of the calculation are shown in appendix B. In figure 2 the mobility depends on the Al content x mainly via (i) the amount of the wavefunction penetration into the barriers (described by the integrals over Ψ_i) and (ii) the factor $[x(1-x)]^{-1}$. The factor $[x(1-x)]^{-1}$ tends to infinity for $x \to 0$ and $x \to 1$ and has a minimum for $x = 0.5$. On the contrary the integrals including Ψ_i cause a monotonic increase with rising x over the total range $0 \leqslant x \leqslant 1$. With growing x, i.e. increasing barrier height, the amount of the electron and hole wavefunction penetration into the alloy barrier decreases. Therefore, the integrals contribute to the variation of the scattering efficiency by a decreasing part of the scattering efficiency with rising x and, thus, this contribution leads to an increase of the mobilities. with growing Al content.

For GaAs QWs of 10 nm and 5 nm widths the 2D electron, hole and ambipolar mobilities are calculated and displayed in figure 3 as a function of the barrier Al content at $T = 100$ K. The full curves show the electron and hole mobilities. The ambipolar mobility is calculated from the electron mobilities μ_e and hole mobilities μ_h according to $\mu_{\mathrm{amb}} = 2(1/\mu_\mathrm{e} + 1/\mu_\mathrm{h})$ and is shown in the diagram by the dotted curves. In figure 3 we observed a strong increase of the mobilities with rising x in the range $0.5 \leqslant x \leqslant 1$. For $x \to 1$ the mobilities tend to infinity since the AlAs barriers cause no BAL scattering. For $0 \leqslant x \leqslant 0.5$ the factor $[x(1-x)]^{-1}$ reveals the reverse dependence on x compared to the integrals describing the penetration of the wavefunctions. For $L_z = 10$ nm and $0 \leqslant x \lesssim 0.04$ the electron mobility decreases with increasing Al content since the factor $[x(1-x)]^{-1}$ dominates. In contrast, for $0.04 \lesssim x \leqslant 0.5$ the electron mobilities increase with growing Al content, since the wavefunction penetration into the barriers (integrals in (2)) dominates. A similar variation is found for the hole mobility and other well widths. The minimum in the mobility versus Al content variation is found to be located at larger x for μ_e compared to μ_h and is further found at higher x for larger well widths.

Furthermore an interesting crossing of μ_e and μ_h is observed in figure 3. In the range of very small x values we find $\mu_\mathrm{e} > \mu_\mathrm{h}$ and for x values exceeding the crossing point we observe the reverse behaviour $\mu_\mathrm{e} < \mu_\mathrm{h}$. Thus, the ambipolar mobility is dominated by the electrons at higher Al contents and by the holes at very small x values. This behaviour is due to the interplay between several effects: (i) the different vertical masses of electrons and holes, (ii) the different variation of the electron and hole masses with x, (iii) the Al-content

dependence of the barrier heights of the conduction and valence band potential wells and (iv) the factor $[x(1-x)]^{-1}$. Two limiting cases can be easily understood. For larger L_z and higher x, i.e. large barrier heights, the amount of wavefunction penetration is larger in the conduction band compared to the valence band. This is due to the fact that the vertical hole masses are considerably larger than the electron masses while the band discontinuities between conduction and valence band are not very different ($\Delta E_c/\Delta E_v = 60/40$, see table 1). Due to this difference in the masses, the penetration of the wavefunctions into the barriers is larger in the conduction-band QW compared to the valence-band QW and we thus obtain $\mu_e < \mu_h$. In the second bordering case ($x \to 0$) the mobilities have to tend to the respective 3D values of alloy scattering in $Al_xGa_{1-x}As$ where we have $\mu_e > \mu_h$.

In 3D alloy materials, however, the variation with x of the disorder scattering process is dominated by $[x(1-x)]^{-1}$ [15–17]. For a constant well width, we expect a transition from 2D to 3D carrier systems, if the Al content tends to zero, i.e., the barrier height shrinks for a constant well width. In this case with $x \to 0$ the potential well characteristics will finally disappear and the entire heterostructure will tend to homogeneous GaAs and, thus, the BAL mobility has to tend to infinity. For comparison, the mobility calculated only under consideration of alloy-disorder scattering [16, 18, 19] for ambipolar carriers in 3D $Al_xGa_{1-x}As$ is also displayed at the bottom of figure 3 by the broken curves for $T = 100$ K. For $x \gtrsim 0.1$ the BAL mobilities are considerably higher than the 3D alloy-disorder scattering mobilities since only a small part of the wavefunction in the barrier participates in the scattering.

Figure 4 depicts the 2D electron, hole and ambipolar mobilities as a function of well width considering only BAL scattering for $x = 0.5$. With increasing well width the scattering rate rises monotonically in the range 1 nm $< L_z <$ 20 nm which is due to the decrease of the wavefunction penetration into the barrier alloy. In the range of $L_z > 1.5$ nm we find $\mu_e < \mu_h$. For very thin QWs in the range below the crossing point we observe the reverse behaviour, $\mu_e > \mu_h$. Since the vertical electron masses exceed the vertical hole masses, the wavefunction of the electrons penetrates more efficiently into the barriers compared to that of the holes and we thus obtain $\mu_e < \mu_h$ for larger well widths. If $L_z \to 0$ the wavefunctions are finally completely delocalized in the $Al_xGa_{1-x}As$ barriers and the 2D electron and hole mobilities will tend to the corresponding 3D mobilities [16, 18, 19]. Since we have $\mu_e > \mu_h$ in 3D $Al_xGa_{1-x}As$ for the alloy scattering mobilities [18, 19], the 2D mobilities reveal the same behaviour for small well widths since a transition between 2D and 3D has to be achieved†. The position of the observed crossing depends mainly on x and L_z as well as on the variation of the masses‡ on x and L_z. The crossing of the theoretical electron and hole mobilities for isolated BAL scattering for narrow QW widths and small x was treated in more detail in this paper, since it is also of physical interest for unipolar transport and to our knowledge has not been reported before.

Theoretical BAL mobilities are calculated using our model and are compared to the experimental data in figure 2. The BAL scattering mobility for 2D carrier systems is given

† Note that this transition from a 2D to a 3D carrier system cannot be fully described by our simple model calculation since pure 2D masses are used and the L_z dependence of the masses is not included. A correct theory has to consider the transition from the 2D to the 3D electronic dispersion relation. Note that the consideration of only one subband leads to deviations for large well widths (between 15 and 20 nm) since the subband separation is reduced with increasing well width. Due to the participation of higher subbands, the carrier system is no longer exactly 2D.

‡ Due to the efficient valence-band mixing in QWs the parallel heavy-hole mass considerably increases with growing parallel wavevectors. A correct description would require the computation of the complex valence band structure as a function of well width, Al content and temperature. These effects are neglected and masses independent of L_z and T are used.

Table 1. Material parameters used for the model calculations. The values for the vertical and parallel valence-band masses (near the Γ point) result from our recent calculation [21] for ternary and quaternary material systems based on the Luttinger–Kohn parameters [22].

Parameter	Description
$E_g^\Gamma(x,T) = (1.519 - 0.08\coth(155/T) - 1) + 1.239(1 - 2.26\times10^{-4}T)x + 0.37x^2)$ eV	Band-gap energy of $Al_xGa_{1-x}As$ at the Γ point calculated from $E_g(x, T = 0\ K)$, $E_g(x, T = 100\ K)$ and $E_g(T, GaAs)$ from [23–26]
$m_e = 0.0665 + 0.0735x$	Electron mass in $Al_xGa_{1-x}As$ [24, 27]
$m_{hh,\perp}^\Gamma = (3 - 0.52x)^{-1}$	Heavy-hole mass of $Al_xGa_{1-x}As$ vertical to the [100] interface at the Γ point [21, 22]
$m_{lh,\perp}^\Gamma = (10.6 - 5x)^{-1}$	Light-hole mass of $Al_xGa_{1-x}As$ vertical to the [100] interface at the Γ point [21, 27]
$m_{hh,\parallel}^\Gamma = (8.7 - 3.88x)^{-1}$	Heavy-hole mass of $Al_xGa_{1-x}As$ parallel to the [100] interface at the Γ point [21, 22][a]
$m_{hh,\parallel} = (2 - 0.35x)/(8.7 - 3.88x)$	Heavy-hole mass of $Al_xGa_{1-x}As$ parallel to the [100] interface for wavevectors $\gg 0$ [21, 22][a]
$m_{lh,\parallel} = (4.9 - 1.64x)^{-1}$	Light-hole mass of $Al_xGa_{1-x}As$ parallel to the [100] interface at the Γ point [21, 22][a]
$a(x,T) = (0.565\,14 + 8.16\times10^{-4}x + 6.4\times10^{-7}T - 1.2\times10^{-7}xT)$ nm	Lattice constant of $Al_xGa_{1-x}As$ calculated from $a(x)$ and $a(T)$ including the thermal expansion coefficient [24]
$V_{0,e} = 0.6$ eV	Electron alloy-disorder scattering potential [28]
$V_{0,h} = 0.4$ eV	Hole alloy-disorder scattering potential; $V_{0,e}$ and $V_{0,h}$ are connected via $\Delta E_c/\Delta E_v$ [20][b]
$\Delta E_c/\Delta E_v = 60/40$	Partition of the band discontinuity between conduction and valence band [20][c]
$r_0 = 0.44a$	Radius of the Wigner–Seitz cell [16]

[a] Due to the efficient valence-band mixing in QWs the parallel heavy-hole mass considerably increases with growing parallel wavevectors. A correct description would require the computation of the complex valence band structure as a function of well width, Al content and temperature. These effects are neglected and masses independent of L_z and T are used.

[b] Note that $V_{0,h} = 0.3$ would decrease the BAL hole mobilities by a factor of 1.3.

[c] Numerous recent publications on band discontinuities in GaAs/AlGaAs heterostructures converge near 60/40 which is very close to the value reported first by Miller *et al* [20].

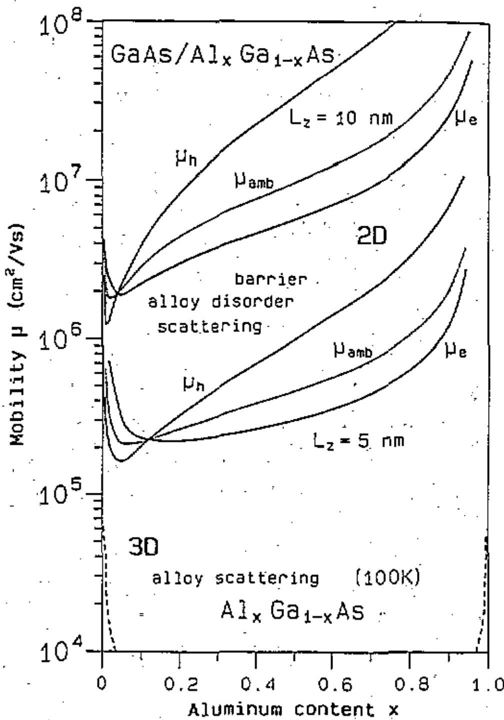

Figure 3. Mobilities calculated considering only BAL scattering as a function of the Al content x for a QW of 5 nm and 10 nm well width (2D) at $T = 100$ K. The electron and hole mobilities (μ_e and μ_h) are given by the full curves and the ambipolar mobilities μ_{amb} are displayed by the dotted curves. For comparison, the alloy-disorder scattering (3D) in bulk $Al_xGa_{1-x}As$ at 100 K is also included by the broken curves.

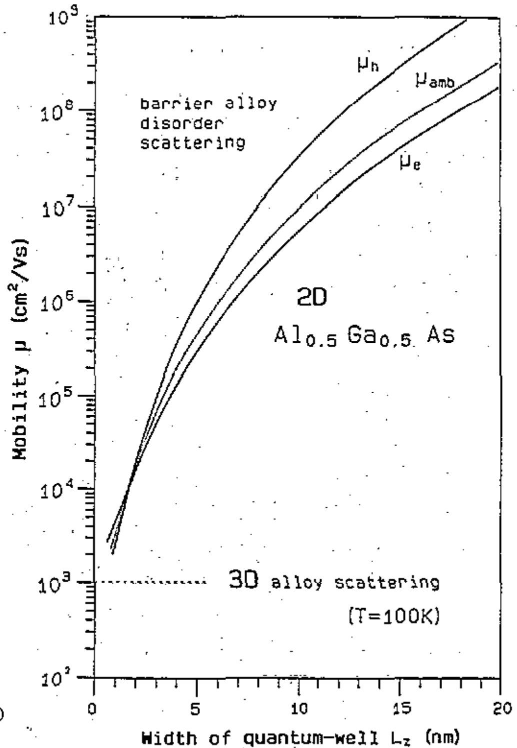

Figure 4. 2D mobilities calculated considering only BAL scattering as a function of the QW width for a barrier Al content x of 0.5 and $T = 100$ K. The electron and hole mobilities (μ_e and μ_h) are given by the full curves and the ambipolar mobilities μ_{amb} are displayed by the dotted curves. For $L_z \rightarrow 0$ the mobility values tend to the 3D mobility values of $Al_{0.5}Ga_{0.5}As$ given by the horizontal broken line.

by the long-dashed curve and is indicated by 'bal'. The calculations shown in figure 2 confirm the observed trend of the experimental mobilities with rising x (figure 1); however, the absolute values of the theoretical mobilities are considerably higher. We will mention two possible interpretations. (i) If excitons also dominate in a temperature range below and close to 100 K, BAL scattering has to be considered also for excitons. This seems to be considerably more complicated than in the case of AC and PO scattering and has not been performed up to now. However, we would expect smaller excitonic BAL mobilities than ambipolar BAL mobilities analogous to AC and PO scattering. This would be consistent with the experiments. Furthermore, we would expect a variation with x very similar to figures 2 and 3. (ii) If excitons do not dominate in the temperature range below or close to 100 K, BAL scattering is expected to play no dominating role, and other scattering mechanisms are expected to reveal a larger influence on the experimental mobilities. A scattering mechanism will be shortly discussed which is closely related to BAL scattering: alloy-cluster scattering [48] in the barriers may influence the mobilities at temperatures close to 100 K. However, alloy clusters can normally be neglected in MBE-grown $Al_xGa_{1-x}As$.

In figure 2 we obtain a slight decrease of the theoretical BAL mobilities with growing temperatures. This decrease is found to be slightly more distinct for larger well widths. In (2) a temperature dependence is included in the following parameters: the lattice constant

$a(x, T)$, the factor $F(T)$, the band gaps $E_g(x, T)$ and the masses. However, in our calculation the temperature dependences of the masses is not included since no reliable data exist so far for the different Al contents required. The dominant factor in the temperature dependence of the BAL scattering mobilities is the penetration efficiency of the wavefunctions into the barriers. If $E_g(x, T) = E_g(\text{GaAs}, T = 0) + E_1(x) + E_2(T)$ is used to approximate the dependence of the band bap on temperature and Al content, the total temperature dependence of $\mu_i(T)$ is very weak and negligible on a logarithmic mobility scale. Such a dependence for $E_g(x, T)$ was used in [7]. We have updated and improved the variation $E_g(x, T)$ in this paper as follows: $E_g(x, T) = E_g(\text{GaAs}, T = 0)+E_1(x)+E_2(T)+E_3(x, T)$ (see table 1). Due to the term $E_3(x, T)$ which includes a product of x and T, a small but noticeable dependence of μ_i results (see figure 2). The temperature dependence is stronger at higher temperature and is very weak at low temperatures, reflecting the weak temperature dependence of the band gaps at low temperatures [25].

All the data given in this paper are calculated for a band discontinuity of $\Delta E_c/\Delta E_v = 0.6/0.4$. For comparison, the mobilities for BAL scattering have also been calculated for $\Delta E_c/\Delta E_v = 0.67/0.33$ [29]. Independent of the well width we found higher μ_e for 0.67/0.33 than for 0.6/0.4 due to the weaker wavefunction penetration into the barriers in the first case. For μ_h the reverse behaviour is observed, due to the stronger wavefunction penetration into the barriers in the first case. The corresponding ambipolar mobilities differ by about 5% for $L_z = 1.5$ nm and by about 2% for $L_z = 10$ nm. Thus, a slight variation of the band discontinuity does not significantly change the results. The results of this comparison are collected in table 2.

Table 2. Comparison of the BAL scattering mobilities for two different band discontinuities and different well widths.

L_z (nm)	μ_e	μ_h	μ_{amb}	$\Delta E_c/\Delta E_v$
10	4 260 000	18 700 000	6 940 000	0.6/0.4
	4 130 000	18 700 000	6 770 000	0.67/0.33
5	249 000	609 000	354 000	0.6/0.4
	231 000	644 000	340 000	0.67/0.33
2.5	28 200	30 500	29 300	0.6/0.4
	24 700	38 200	30 000	0.67/0.33
1.5	9 470	6 170	7 470	0.6/0.4
	7 880	7 740	7 800	0.67/0.33

In the following, scattering mechanisms which contain adjustable parameters will be considered: firstly, different kinds of impurity scattering, secondly, IR scattering.

(i) Scattering at ionized impurities [30–33] located in the QWs of smaller well width ($L_z \lesssim 12$ nm) provides a growing scattering probability with increasing well width (e.g. $\mu_{im} \simeq T/L_z$ for 2D carrier systems according to [32], or the more complicated dependence on L_z and T according to [30] and [31]). In contrast, our experimental mobility increases with rising L_z. Furthermore, our samples are not intentionally doped and the theoretical mobility values for the ionized-impurity scattering estimated from residual impurity concentrations considerably exceed the experimental data.

(ii) Impurities may also be accumulated at QW interfaces [30, 33]. However, an important experimental observation indicates that the corresponding interface-impurity scattering most probably plays no important role in our QWs: growth interruption at the interfaces enables the incorporation of impurities at the interfaces; thus, these samples should show lower

mobilities compared to continuously grown samples if scattering at ionized impurities strongly contributes. However, we observe the opposite behaviour, i.e. higher mobilities in the growth-interrupted QWs [34].

(iii) Remote-impurity scattering or barrier-impurity scattering [3, 30–33] from nominally undoped barriers reveals mobilities increasing with rising well widths which is consistent with our experimental data. However, for comparable residual impurity concentrations in the QWs and the barriers, smaller scattering rates would be obtained for barrier-impurity scattering compared to well-impurity scattering. Even if the impurity concentrations in the barriers are assumed to be higher (in reasonable ranges) than in the wells, the theoretical mobilities for the barrier-impurity scattering remain higher than the experimental mobility data. Therefore, in our opinion remote-impurity scattering most probably plays a minor role in our samples.

(iv) Impurities may also have a non-uniform distribution (impurity clusters) which leads to space charges which may affect the mobility (space-charge mobility) [17, 35]. Since the theoretical mobility decreases with rising temperature, this scattering mechanism cannot explain the strong increase of the experimental mobilities with low rising temperatures and only may contribute at temperatures close to about 100 K. Impurity clusters in the QWs would provide a well width variation of the mobility which is the reverse of that observed in the experiment. Barrier-impurity-cluster scattering mobilities increase with growing well widths; however, an unusually high concentration and/or area of the space-charge scattering centres would be required to explain the experimental data. In addition, impurity clusters can normally be neglected in MBE-grown structures.

We think that, in addition, all the different scattering processes (i)–(iv) of excitons by charged impurities are weakened by the bipolar nature of the e–h pairs, i.e. the partial self-screening. Thus, we believe that the influence of the different modifications of impurity scattering is overcompensated by IR scattering in our samples. In the following the strong increase of the experimental low-temperature diffusivities and mobilities with growing well width is discussed and attributed to efficient IR scattering. Geometrical IR parameters are determined by fitting results of IR model calculations to our experimental data.

IR scattering is known to enable a strong reduction of the lateral mobility with decreasing well width [2, 4, 5, 9, 30, 33, 36]. These results were measured close to 2 K or calculated for 0 K. In the temperature range $10 \text{ K} < T < 40 \text{ K}$ we observed an increase of the experimental e–h-pair mobility with decreasing temperature below 40 K [13, 14]. This reincrease is most probably caused by non-equilibrium effects in the carrier and phonon system [13, 14]. Thus, in our sample for $T \lesssim 30$ K the mobility decrease caused by IR scattering is hidden by these non-equilibrium effects leading to a mobility enhancement. Due to this observation we are unable to use helium-temperature mobility data to discuss IR scattering processes. Therefore we use experimental data for $T = 40$ K and slightly higher temperatures (40–60 K for $L_z = 1.5$, 2.5 and 5 nm as well as 25–40 K for $L_z = 10$ nm) to fit the results of IR model calculation to our experimental data.

For the characterization of the interface morphology, we use an IR model containing two variable parameters: an average terrace height Δ and an average terrace length Λ. IR strongly influences both lateral carrier mobilities [2, 4, 33, 36] and linewidths [37–39] of photoluminescence spectra. For $T = 10$ K we have observed linewidths of 6.2, 2, 1 and 0.9 meV for QW widths of $L_z = 1.5$, 2.5, 5 and 10 nm, respectively. The most important contribution to the linewidths in photoluminescence or absorption spectra of carriers confined in a QW has been attributed to IR [37–39] and a smaller contribution has been related to alloy composition fluctuations [37, 38]. The linewidth part that can be related to IR is obtained from the measured values by the subtraction of the BAL linewidth part according to [37]

and [38]. Note that for small well widths (below about 10 nm) the linewidth broadening caused by IR is dominated by the terrace height Δ and is much larger than the linewidth broadening caused by BAL. The average terrace length and height included in our IR model simultaneously have to describe both the experimental mobility and linewidth data. In a simple linewidth model the terrace height Δ varies in large steps (e.g. 1, 2 or 3 monolayers) and this parameter Δ is almost predefined by the linewidth, since the dependence of the linewidth on the terrace length Λ is much weaker. We have varied the average length Λ and height Δ in our model for a given well width to obtain the best description of all our experimental linewidth and mobility data by curve fitting. In the low-temperature range IR scattering is expected to dominate, but AC scattering also contributes and has to be considered if the experimental mobility data are used to determine Δ and Λ. According to Mattheissen's rule the inverse experimental mobility $(\mu_{exp})^{-1}$ can be approximated by the sum of the inverse experimental mobilities of IR and AC scattering:

$$1/\mu_{exp} = 1/\mu_{ir} + 1/\mu_{ac}. \tag{3}$$

Note that the correction to the IR mobility μ_{ir} by μ_{ac} via (3) is very small, since for $T = 40$ K the mobility difference between the experimental values and the theoretical mobilities corresponding to these scattering mechanisms shown in figure 2 is vary large. Thus, we determine the 'residual' mobility μ_{ir} from (3). This residual mobility μ_{ir} is displayed in figure 5 as a function of well width for $T = 40$ K by the filled circles.

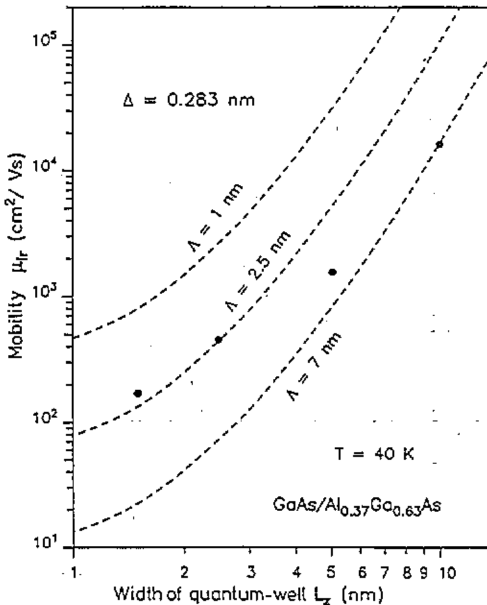

Figure 5. IR mobility part μ_{ir} of the mobility as a function of well width for $x = 0.37$. The values for the symbols are determined from the measured data in consideration of the contribution of the already determined scattering parts for BAL scattering and AC scattering. The theoretical variations are displayed as broken lines for different terrace lengths Λ.

In our calculation of the IR scattering time, we use approaches known from the literature [36, 40, 41, 33]. In most publications the IR mobility is calculated for $T = 0$ K. In order to enable a comparison between experimental data and mobilities obtained from IR model calculations we have to approximate the temperature dependence close to 40 K. We approximate a temperature variation of the scattering time by performing the energy averaging of the scattering rates with respect to the Boltzmann distribution and the density of states. Some details of the calculation are shown in appendix C. The calculated temperature dependence yields a good description of the mobility variation with T only

for low temperatures. For higher temperatures our theoretical IR mobility is too weak to describe the strong thermal increase observed in the experiment at $T > 60$ K. Therefore we do not include the temperature dependence of the calculated IR mobilities in figure 2.

The calculated IR-scattering-limited mobilities are displayed in figure 5 by the broken lines for $T = 40$ K and $\Delta = 0.283$ nm as a function of well width. We obtain a strong increase of the mobilities with rising well width. Note that we obtain no power-law dependence $\mu \simeq L_z^w$ for small well widths, which would result in straight lines in the double-logarithmic plot of figure 5. For the sample having an Al content of 0.37 we obtain an average step height of $\Delta = 0.283$ nm (one monolayer) for all QW widths and an average terrace length increasing with growing well width is suggested according to figure 5. These values are comparable to values reported in the literature for similar structures [2, 4, 5, 9]. We obtain $\Lambda = 2.2$, 2.5, 5 and 7 nm for $L_z = 1.5$, 2.5, 5 and 10 nm, respectively. In a sample of $x = 0.5$ we obtain $\Lambda \simeq 6$, 12 and 13 nm for $L_z = 4$, 8 and 15 nm, respectively. This is comparable to the value of $\Lambda = 10$ nm published by Basu and Partha Ray [9] for all three QW widths for our sample. These authors have also calculated IR scattering limited mobilities of excitons and compared their theoretical data to our experimental data published in [7] for $x = 0.5$. A well width dependence for Λ is proposed for the terrace length to improve the agreement between experimental and theoretical data in our paper. The increase of the terrace length with growing well width may be due to enhanced terrace lengths at the interface which is grown second. Note that our experimental method averages over both interfaces and the observed increase of the terrace length with growing well width is not influenced by a moderate change in the contributions of the other scattering mechanisms according to (3).

At low temperatures localization effects [6, 42–44] may also considerably reduce the lateral diffusion and mobility of excitons in QWs. In $GaAs/Al_xGa_{1-x}As$ QWs the localization of excitons was studied in detail at 5 K [6] and $D = 1$ cm^2 s^{-1} ($D = 15$ cm^2 s^{-1}) was found for localized (non-localized) excitons, respectively, for $L_z = 21$ nm. We find a good agreement of the non-localized-exciton diffusivity value with our extrapolated experimental data ([7] in this paper). For smaller well widths which we consider here, localization effects may be more important; however, they will be most probably less important for the higher temperatures which we consider ($T > 40$ K). The inclusion of localization effects would increase the residual mobility μ_{ir} values in figure 5 mainly for smaller L_z, which would result in a stronger dependence of the terrace length on L_z. For very small well width ($L_z = 1.5$ or 2.5 nm) we would expect lower effective diffusivities if carrier trapping and re-emission dominated the motion than observed in the experiment. However, localization may slightly influence our mobility data.

4. Conclusions

We have used microstructured masks on top of QW heterostructures to probe the lateral transport of e–h pairs as a function of well width, Al content and temperature. The experimental carrier mobility is found to strongly increase with both growing well width and Al content. The variation of the experimental e–h-pair mobilities is compared to model calculations based on different scattering mechanisms. The variation of the experimental mobility with temperature and well width can be described by IR, AC and PO scattering. The contributions of BAL scattering are found to be rather weak and only noticeable for very narrow QW widths. The strong mobility increase with growing well width at low temperatures is most probably due to efficient IR scattering. The interface terrace lengths and

heights in the model are approximately determined by a comparison of model calculations and experimental data for $T \simeq 40$ K.

Acknowledgments

We wish to thank T Kuhn, M Pilkuhn, R Sauer, S Hansmann and M Morohashi for stimulating discussions. The authors are grateful to H P Meier for the MBE growth of the QW sample ($x = 0.3$) the results of which are shown among others in figure 1. The financial support of the Deutsche Forschungsgemeinschaft (SFB 329) and the Stiftung Volkswagenwerk are gratefully acknowledged.

Appendix A. Finite-barrier potential well

To determine energy eigenstates and wavefunctions of a symmetric finite QW of width L_z the Schrödinger equation has to be solved. This has to be performed for both the conduction- and the valence-band potential wells. The band-edge energy offsets which cause the confinements of electrons and holes are denoted by ΔE_c and ΔE_v respectively. The sum of the offsets $\Delta E_c + \Delta E_v$ is given by the difference of the band-gap energies of the barrier and the well $E_g(Al_xGa_{1-x}As) - E_g(GaAs)$. The band discontinuity quotient $\Delta E_c/\Delta E_v$ gives the partition of the total offset between the conduction and the valence band. In the following the subscript i means e in the case of electrons and h in the case of holes such as, e.g., in the case of the barrier masses $m_{b,i}$ or the QW masses $m_{q,i}$. This problem finally leads to the following equation

$$m_{b,i,\perp}\alpha_i = m_{q,i,\perp}\beta_i \cot(\alpha_i L_z/2) \tag{A1}$$

which has to be solved for both electrons and holes. The abbreviations α_i and β_i include the energy of the ground state E_i (the difference between the GaAs band edge and the first subband) and are given by

$$\alpha_i^2 = 2m_{q,i,\perp}E_i/\hbar^2 \qquad \beta_i^2 = 2m_{b,i,\perp}(\Delta E_i - E_i)/\hbar^2. \tag{A2}$$

The subscript $\perp$ indicates that the masses vertical to the hetero-interfaces are used.

Appendix B. BAL scattering rate

Alloy fluctuations were reported to influence the carrier motion like alloy-disorder scattering in 3D alloy materials [15–17] and 2D alloy materials [28, 45], i.e. QW heterostructures in which an alloy is used for the well, such as InGaAs/InP. However, alloy fluctuations also may influence the lateral carrier motion in QW systems having alloy barriers such as GaAs/AlGaAs [3, 28, 30, 32, 36, 46].

In the literature BAL scattering for electrons is calculated for various geometrical conditions using different approximations [3, 28, 30, 33, 36, 46]. In [7] and [47] we have briefly described our simple model calculation of the mobility under consideration of BAL scattering. The BAL scattering efficiency is mainly determined by the penetration of the electron and hole wavefunctions into the QW barriers. The QW interfaces are located at $z = \pm\frac{1}{2}L_z$. In both barriers (i.e. for $|z| > \frac{1}{2}L_z$) the wavefunctions reveal an exponential decay in space (see the last term in (A3) below). Solving (A1) numerically the QW energy

eigenstates (and thus α_i and β_i) can be obtained. Using the parameters α_i and β_i the z dependence of the wavefunctions in the barriers can be given explicitly:

$$\Psi_i^{\pm}(z) = [1/2\beta_i + \tfrac{1}{2}L_z/\cos^2(\alpha_i L_z/2) + m_{\mathrm{q},i,\perp}\beta_i/m_{\mathrm{b},i,\perp}\alpha_i^2]^{-0.5}\exp[\beta_i(\tfrac{1}{2}L_z \pm z)] \quad \text{for } |z| > \tfrac{1}{2}L_z. \tag{A3}$$

The first term in (A3) gives the amplitudes of the wavefunction at $|z| = \pm\frac{1}{2}L_z$ and, thus, is very important for BAL scattering. According to (A3), the electron or hole well wavefunctions $\Psi_i(z)$ contain the energy of the ground state, the well width, the masses in the barriers and wells in the direction perpendicular to the QW interfaces, as well as the respective barrier heights. The barrier height ΔE_c (ΔE_v) in the conduction (valence) band is included via α_i (β_i). Thus, the quantity $\Delta E_c/\Delta E_v$ balances how strongly BAL scattering is influenced by the electron wavefunction or the hole wavefunction penetration into the barriers, respectively.

We calculate the BAL scattering rate for one subband, neglecting screening effects and including the occupation probability for the final states of the scattering process. At the carrier densities considered here, only the lowest subband of each well is occupied and inter-subband scattering can be neglected.

In equations (A4)–(A7) below we omit the index i for electrons and holes. We assume the Al atoms to be situated at $\boldsymbol{R}_j$ and approximate their potential V_{Al} to be constant within the Wigner–Seitz radius r_0, i.e. for $|\boldsymbol{r} - \boldsymbol{R}_j| \leqslant r_0$ and to be zero outside (analogous for the potential V_{Ga} of the Ga atoms). The averaged potential has to be zero: $\bar{V} = xV_{\mathrm{Al}} + (1-x)V_{\mathrm{Ga}} = 0$ with $V_{\mathrm{Al}} - V_{\mathrm{Ga}} = V_0$, the BAL scattering potential. Thus we obtain include the Wigner–Seitz cell the constant potentials

$$V_{\mathrm{Al}} = (1-x)V_0 \qquad V_{\mathrm{Ga}} = -xV_0 \qquad \text{for } |\boldsymbol{r} - \boldsymbol{R}_j| \leqslant r_0. \tag{A4}$$

A comparable *ansatz* was performed by Harrison and Hauser [16] for 3D alloy-disorder scattering and is also used in the calculation of 2D BAL scattering [36, 28]. In the following, $\boldsymbol{k}$ ($\boldsymbol{k}'$) gives the wavefactors of the initial (final) state of the scattering process in the plane of the hetero-interface. The scattering angle between $\boldsymbol{k}$ and $\boldsymbol{k}'$ is given by Θ. The transition rate $S(\boldsymbol{k}, \boldsymbol{k}')$ is given by

$$S(\boldsymbol{k}, \boldsymbol{k}') = (2\pi/\hbar)|V_{\boldsymbol{k}\boldsymbol{k}'}|^2\delta[(\hbar^2/2m_{\parallel})(k^2 - k'^2)]. \tag{A5}$$

The contribution of the atom j to the scattering potential between the initial and final state is found to be

$$V_{\boldsymbol{k}\boldsymbol{k}'}^{(j)} = A^{-1}\exp[\mathrm{i}(\boldsymbol{k}-\boldsymbol{k}')\cdot\boldsymbol{R}_j]V_j\int_{z_j-r_0}^{z_j+r_0}\mathrm{d}z\int_0^{[r_0^2-(z-z_j)^2]^{0.5}} r_\parallel'\mathrm{d}r_\parallel'\int_0^{2\pi}\mathrm{d}\varphi\exp[\mathrm{i}(\boldsymbol{k}-\boldsymbol{k}')\cdot\boldsymbol{r}_\parallel']|\Psi(z)|^2 \tag{A6}$$

where $\boldsymbol{r}_\parallel'$ gives the radius vector in the plane of the hetero-interface. The total potential $V_{\boldsymbol{k}\boldsymbol{k}'}$ of all atoms for the scattering process between the initial and final state is obtained by summation over the contributions of all atoms. Furthermore we use the approximation $|\boldsymbol{k} - \boldsymbol{k}'|r_0 \ll 1$. Since the atoms are distributed randomly only diagonal elements remain.

$$|V_{\boldsymbol{k}\boldsymbol{k}'}|^2 = \sum_j(\pi V_j/A)^2|I(z_j)|^2 \qquad \text{with } I(z_j) = \int_{-r_0}^{r_0}|\Psi_i(z+z_j)|^2(r_0^2 - z^2)\,\mathrm{d}z. \tag{A7}$$

The summation spreads into a summation over the Al atoms and a summation over the Ga atoms. We use $n_{\mathrm{Al}} = xn_0$ and $n_{\mathrm{Ga}} = (1-x)n_0$ for the concentration of the respective atoms

with $n_0 = 4/a^3$. $n_0 = 4/a^3$ gives the number of As atoms in the unit volume including the lattice constant a. The scattering rate depending on the wavevector of the initial state is given by

$$\tau_i^{-1}(\boldsymbol{k}) = \int_0^\infty \mathrm{d}\boldsymbol{k}' S_i(\boldsymbol{k}, \boldsymbol{k}')(1 - \cos\Theta) = \frac{\pi}{2\hbar} n_0 V_{0,i}^2 2 \int_{L_z/2}^\infty \mathrm{d}z_j |I(z_j)|^2 x(1-x) \int_0^{2\pi} \mathrm{d}\varphi$$
$$\times \int_0^\infty \mathrm{d}k'\, k'(1 - \cos\varphi)\delta\left(\frac{\hbar^2}{2m_{i,\mathrm{b},\parallel}}(k^2 - k'^2)\right). \tag{A8}$$

We now distinguish between the conduction and valence band via the index i. The energy conservation of the elastic scattering process is provided by the δ function. The probability that the final state of the scattering is not occupied is given by $(1 - f_i(E_k))$ which is taken into account in (A9) below where the scattering rate is averaged over the energy $\langle\rangle_E$ with respect to the Fermi distribution function $f_i(E_k)$:

$$\langle\tau^{-1}\rangle_{E,i} = \int \mathrm{d}E\, Z(E) f_i(E_k)(1 - f_i(E_k))\tau_i^{-1}(\boldsymbol{k}) \Big/ \int \mathrm{d}E\, Z(E) f_i(E)_k). \tag{A9}$$

(A9) further includes the 2D density of states $Z_i(E)$ of the first subband. Finally we obtain

$$\tau_i^{-1} = \frac{\pi^2}{\hbar^3} n_0 m_{i,\mathrm{q},\parallel} V_{0,i}^2 2 \int_{L_z/2}^\infty \left(\int_{-r_0}^{r_0} |\Psi_i(z + z_j)|^2 (r_0^2 - z^2)\,\mathrm{d}z\right)^2 x(1-x)F(T)\,\mathrm{d}z_j. \tag{A10}$$

The temperature dependence resulting from the energy-averaging in (A9) is denoted by $F(T)$. The Al content x is included in the barrier masses, the energy eigenvalues and thus in Ψ_i, in n_0 and the expression $x(1-x)$. In contrast, the well width dependence is contained in the energy eigenvalues of the potential wells, i.e. in the wavefunctions and in the integration borders. Note, that the scattering rate is also sensitive to the partition of the band discontinuity between conduction and valence bands since the energy eigenvalues depend on the barrier heights in the conduction and valence bands, respectively.

The BAL-scattering-limited mobility for e–h pairs is calculated starting from the scattering rates given for electrons and holes in (A10) as a function of x and L_z and using the material parameter values given in table 1. The mobility for the electrons and holes is obtained from $\mu_i = \tau_i e/m_{\mathrm{opt},\parallel,i}$ where the optical GaAs masses parallel to the interfaces are included (see (2)). The ambipolar mobility is calculated from the electron mobilities μ_e and hole mobilities μ_h according to $\mu_{\mathrm{amb}} = 2(1/\mu_\mathrm{e} + \mu_\mathrm{h})$.

Appendix C. Interface roughness scattering rate

We consider a rectangular potential well with finite barriers to calculate IR scattering. Since first, low carrier densities are considered in our experiment and second, IR scattering processes dominate in the temperature range < 100 K, we can restrict our model to the first electron and the first heavy-hole subbands. The two hetero-interfaces which define the QW reveal an independent roughness characterized by a terrace height Δ and a terrace length Λ. According to Prange and Nee [40] the local deviations of a hetero-interface from a perfect plane can be described by an autocorrelation function

$$\langle\delta(\boldsymbol{r})\delta(\boldsymbol{r}')\rangle_\epsilon = \Delta^2 \exp(-|\boldsymbol{r} - \boldsymbol{r}'|^2/\Lambda^2). \tag{A11}$$

In (A11) $\boldsymbol{r}$ and $\boldsymbol{r}'$ denote space vectors in the xy plane (the plane of the hetero-interface). This Gaussian distribution of the terrace lengths leads to a potential fluctuation which was described by Price and Stern [41] and Gold [33] by a random potential:

$$\begin{aligned}\langle|U_{\rm ir}(\mathrm{q}, \Delta E_i, L_z)|^2\rangle_{\epsilon,i} &= 2\pi\Delta^2\Lambda^2\exp(-\tfrac{1}{4}|\boldsymbol{k}-\boldsymbol{k}'|^2\Lambda^2)[16\hbar^4/(m_{\mathrm{q},i,\perp}L_z^3)^2]\\ &\quad\times(1+\sin(L_z\alpha_i)/L_z\alpha_i+\cos^2(\tfrac{1}{2}L_z\alpha_i)/\tfrac{1}{2}L_z\beta_i)^2\\ &\quad\times[(1-m_{\mathrm{b},i,\perp}/m_{\mathrm{q},i,\perp})(\tfrac{1}{2}L_z\alpha_i)^2\sin^2(\tfrac{1}{2}L_z\alpha_i)+(m_{\mathrm{q},i,\perp}L_z^2\Delta E_i/2\hbar^2)\\ &\quad\times\cos^2(\tfrac{1}{2}L_z\alpha_i)]^2.\end{aligned}\qquad\text{(A12)}$$

The subscript ir is the abbreviation for interface roughness and the index i means e and h for electrons and holes, respectively. $\langle\rangle_\epsilon$ denotes the ensemble averaging and $\boldsymbol{k}(\boldsymbol{k}')$ give the wavevectors of the initial (final) state of the scattering. The factor 2 originates from the consideration of the two interfaces. α_i and β_i contain the energy of the ground state E_i according to (A2) and the barrier Al content x. The momentum relaxation time for the scattering process can be calculated using (A12)

$$\tau_{\mathrm{ir},i}^{-1}(E)=\frac{2\pi}{\hbar}\int_{-\infty}^{\infty}\mathrm{d}^2\boldsymbol{k}'\langle|U_{\rm ir}(\boldsymbol{k}-\boldsymbol{k}')|\rangle_{\epsilon,i}^2\delta(E_{\boldsymbol{k}}-E_{\boldsymbol{k}'})(1-\cos\Theta).\qquad\text{(A13)}$$

The delta-function provides the energy conservation between the initial energy $E_{\boldsymbol{k}}$ and the final energy $E_{\boldsymbol{k}'}$. The energy averaging is performed for the electron and hole subbands separately with respect to the distribution function. This step provides to a first approximation the temperature dependence of IR scattering. The Fermi distribution is approximated by the Boltzmann distribution $b_i(E)$:

$$\left\langle\frac{1}{\tau_{\mathrm{ir},i}(E)}\right\rangle_E=\int_{E_{i(\mathrm{C,V})}}^{\infty}\tau_{\mathrm{ir},i}^{-1}(E)b_i(E)Z_i(E)\,\mathrm{d}E\bigg/\int_{E_{i(\mathrm{C,V})}}^{\infty}b_i(E)Z_i(E)\,\mathrm{d}E.\qquad\text{(A14)}$$

The integration starts at the band-edge energies $E_{i(\mathrm{C,V})}$ of the conduction and valence bands respectively. (A14) includes the 2D density of states $Z_i(E)$ of the first subband as well as the Boltzmann distribution $b_i(E)$ which contains the Fermi level $E_{\mathrm{F},i}$

$$Z_i=m_{i,\parallel}/\pi\hbar\qquad b_i=\exp[-(E-E_{\mathrm{F},i})/k_{\mathrm{B}}T].\qquad\text{(A15)}$$

Finally the respective mobilities are calculated from the scattering rates analogous to BAL scattering.

References

[1] English J H, Gossard A C, Wiegmann W, Bondal R and Baldwin K 1987 *Appl. Phys. Lett.* **50** 1826–28
[2] Sakaki H, Noda T, Hirakawa K, Tanaka M and Matsusue T 1987 *Appl. Phys. Lett.* **51** 1934–6
[3] Walukiewicz W, Ruda H E, Lagowski J and Gatos H 1984 *Phys. Rev.* B **30** 4571–82
[4] Gottinger R, Gold A, Abstreiter G, Weimann G and Schlapp W 1988 *Europhys. Lett.* **6** 183–88
[5] Wataya M, Goto H, Sawaki N and Akasaki I 1989 *Japan. J. Appl. Phys.* **28** 1934–8
[6] Hegarty J and Sturge M D 1985 *J. Opt. Soc. Am.* B **2** 1143–54
[7] Hillmer H, Forchel A, Hansmann S, Morohashi M, Lopez E, Meier H P and Ploog K 1989 *Phys. Rev.* B **39** 10901–12
[8] Smith L M, Preston J S, Wolfe J P, Wake D R, Klem J, Henderson T and Morkoç H 1989 *Phys. Rev.* B **39** 1862–70
Wolfe J P, Yoon H W, Wake D R and Morkoç H 1992 *Semicond. Sci. Technol.* **7** B240–2
[9] Basu P K and Partha Ray 1991 *Phys. Rev.* B **44** 1844–9

[10] Akiyama H, Natsusue T and Sakaki H 1993 *Ultrafast Electronics and Optoelectronics Conf. (San Francisco, 1993)*
[11] Bacher G, Kovac J, Streubel K, Schweizer H and Scholz F 1993 *Phys. Rev.* B **45** 9136–44
[12] Schneider H and von Klitzing K 1988 *Phys. Rev.* B **38** 6160–5
[13] Hillmer H, Forchel A, Tu C W and Sauer R 1992 *Semicond. Sci. Technol.* **7** B235–9
[14] Hillmer H and Tu C W 1993 *Appl. Phys.* A **56** 445–8
[15] Nag B R 1980 *Electron Transport in Compound Semiconductors* vol 11 of (*Springer Series in Solid-State Sciences, 11*) ed H-J Queisser (Berlin: Springer)
[16] Harrison J W and Hauser J R 1976 *Phys. Rev.* B **13** 5347–50
[17] Saxena A K 1981 *Phys. Rev.* B **24** 3295–302
[18] Saxena A K and Gurumurthy K S 1982 *J. Phys. Chem. Solids* **43** 801–8
[19] Masa K, Tokumitsu E, Konagai E and Takahashi K 1983 *J. Appl. Phys.* **54** 5785–92
[20] Miller R C, Kleinmann D A and Gossard A C 1984 *Phys. Rev.* B **29** 7085–7
[21] Hillmer H 1991 *Technical Report DBP Telekom* FI 65 TB 29 E, pp 1–17
[22] Luttinger–Kohn parameters are taken from
Shanabrook B V, Glembocki O J, Broido D A and Wang W I 1989 *Phys. Rev.* B **39** 3411–4
Lawaetz P 1971 *Phys. Rev.* B **4** 3460–7
[23] Wei S-H and Zunger A 1988 *J. Appl. Phys.* **63** 5794–804
[24] Hellwege K H (ed) 1982 *Landolt–Börnstein, New Series* vol 17 (Berlin: Springer) part a
Madelung O (ed) 1987 *Instrinsic Properties of Group IV Elements and III–V, II–VI and I–VII Compounds* (Berlin: Springer) pp 218, 222–4, 234, 247
[25] O'Donnel K P and Chen X 1991 *Appl. Phys. Lett.* **58** 2924–6
[26] Lee H J, Juravel L Y, Woodley L Y and Spring-Thorpe J C 1980 *Phys. Rev.* B **21** 659
[27] Adachi S 1985 *J. Appl. Phys.* **58** R1–29
[28] Ogale S B and Madhukar A 1984 *J. Appl. Phys.* **56** 368–74
[29] Moore K J, Dawson P and Foxon C T 1988 *Phys. Rev.* B **38** 3368–74
[30] Guillemot C, Baudet M, Gauneau M and Regreny A 1987 *Phys. Rev.* B **35** 2799–807
[31] Ogale S B and Madhukar A 1984 *J. Appl. Phys.* **55** 483–86
[32] Lee J, Spector H N and Arora V K 1983 *Appl. Phys. Lett.* **42** 363–65
[33] Gold A 1989 *Z. Phys.* B **74** 53–65
[34] Hillmer H, Forchel A, Sauer R and Tu C W 1990 *Phys. Rev.* B **42** 3220–3
[35] Weissberg L R 1962 *J. Appl. Phys.* **33** 1817–21
[36] Ando T 1982 *J. Phys. Soc. Japan* **51** 3900–7
[37] Singh J and Bajaj K K 1985 *J. Appl. Phys.* **57** 5433–7
[38] Basu P K 1990 *Appl. Phys. Lett.* **56** 1110–12; 1991 *Phys. Rev.* B **44** 8798–801
[39] Weisbuch C, Dingle R, Gossard A C and Wiegmann W 1981 *Solid State Commun.* **38** 709–12
[40] Prange R E and Nee T W 1968 *Phys. Rev.* **168** 779–86
[41] Price P and Stern F 1983 *Surf. Sci.* **132** 577–93
[42] Mott N F and Davis E A 1979 *Electronic Processes in Noncrystalline Materials* 2nd edn (Oxford: Clarendon)
Anderson P W 1983 *Physica* B+C **117–8B** 30
[43] Cohen M H, Fritzsche H and Ovshinsky S R 1969 *Phys. Rev. Lett.* **22** 1065
Hegarty J, Tai K and Tsang W T 1988 *Phys. Rev.* B **38** 7843–5
[44] Schnabel R F, Zimmermann R, Bimberg D, Nickel H, Lösch R and Schlapp W 1992 *Phys. Rev.* B **46** 9873–6
Bastard G, Delalande C, Meynadier M H, Frijlink P M and Voos M 1984 *Phys. Rev.* B **29** 7042–4
[45] Brum J A and Bastard G 1985 *Solid State Commun.* **53** 727–30
[46] Sanghamitra Mukhopadhyay and Nag B R 1992 *Appl. Phys. Lett.* **60** 2897–9
[47] Hillmer H, Hansmann S and Forchel A 1993 *Phys. Rev.* B **47** 6863
[48] Ohno H, Luo J K, Natsuzaki K and Hasegawa H 1989 *Appl. Phys. Lett.* **54** 36–8